Isolated massive star candidates in NGC 4242 with GULP

Pietro Facchini ©¹, Eva K. Grebel ©¹, Anna Pasquali ©¹, Elena Sabbi ©^{2,3}, Beena Meena ©³, Varun Bajaj³, John S. Gallagher III ©⁴, Bruce G. Elmegreen ©⁵, Luciana Bianchi ©⁶, Angela Adamo ©⁷, Daniela Calzetti ©⁸, Michele Cignoni ©^{9,10,11}, Paul A. Crowther ©¹², Jan J. Eldridge ©¹³, Mario Gennaro ©³, Ralf S. Klessen ©^{14,15,16,17}, Linda J. Smith ©³, Aida Wofford ©¹⁸, and Peter Zeidler ©¹⁹

- Astronomisches Rechen-Institut, Zentrum für Astronomie der Universität Heidelberg, Mönchhofstr. 12-14, D-69120 Heidelberg, Germany
 - email:pietro.facchini@stud.uni-heidelberg.de
- Gemini Observatory/NSFs NOIRLab, 950 N. Cherry Ave., Tucson, AZ 85719, USA
- ³ Space Telescope Science Institute, 3700 San Martin Dr, Baltimore, MD 21218, USA
- Department of Astronomy, University of Wisconsin-Madison, 475 North Charter St. Madison, WI 53706 USA
- ⁵ Katonah, NY 10536, USA
- ⁶ Dept. of Physics and Astronomy, the Johns Hopkins University
- Department of Astronomy, Oskar Klein Centre, Stockholm University, AlbaNova University Center, SE-106 91 Stockholm, Sweden
- Department of Astronomy, University of Massachusetts Amherst, 710 North Pleasant Street, Amherst, MA 01003, USA
- ⁹ Dipartimento di Fisica, Università di Pisa, Largo Bruno Pontecorvo 3, 56127, Pisa, Italy
- ¹⁰ INFN, Largo B. Pontecorvo 3, 56127, Pisa, Italy
- INAF Osservatorio di Astrofisica e Scienza dello Spazio di Bologna, Via Piero Gobetti 93/3, 40129, Bologna, Italy
- ¹² Department of Physics & Astronomy, University of Sheffield, Hounsfield Road, Sheffield, S3 7RH, United Kingdom
- Department of Physics, The University of Auckland, Private Bag 92019, Auckland, New Zealand
- ¹⁴ Universität Heidelberg, Zentrum für Astronomie, Institut für Theoretische Astrophysik, Albert-Ueberle-Str. 2, 69120 Heidelberg, Germany
- Universität Heidelberg, Interdisziplinäres Zentrum für Wissenschaftliches Rechnen, Im Neuenheimer Feld 225, 69120 Heidelberg, Germany
- Harvard-Smithsonian Center for Astrophysics, 60 Garden Street, Cambridge, MA 02138, U.S.A.
- ¹⁷ Elizabeth S. and Richard M. Cashin Fellow at the Radcliffe Institute for Advanced Studies at Harvard University, 10 Garden Street, Cambridge, MA 02138, U.S.A.
- ¹⁸ Instituto de Astronomía, Universidad Nacional Autónoma de México, Unidad Académica en Ensenada, Km 103 Carr. Tijuana-Ensenada, Ensenada 22860, México
- AURA for the European Space Agency (ESA), ESA Office, Space Telescope Science Institute, 3700 San Martin Drive, Baltimore, MD 21218, USA

Received XXX; accepted YYY

ABSTRACT

Context. There is considerable debate on how massive stars form, including whether a high-mass star must always form with a population of low-mass stars or whether it can also form in isolation. Massive stars found in the field are often considered to be runaways from star clusters or OB associations. However, there is evidence in the Milky Way and the Small Magellanic Cloud of high-mass stars that appear isolated in the field and cannot be related to any known star cluster or OB association. Studies of more distant galaxies have been lacking so far.

Aims. In this work, we identified massive star candidates that appear isolated in the field of the nearby spiral galaxy NGC 4242 (distance: 5.3 Mpc), to explore how many candidates for isolated star formation we find in a galaxy outside the Local Group.

Methods. We identified 234 massive ($M_{ini} \ge 15M_{\odot}$) and young (≤ 10 Myr) field stars in NGC 4242 using the Hubble Space Telescope's Solar Blind Channel of the Advanced Camera for Surveys, the UVIS channel of the Wide Field Camera 3 from the Galaxy UV Legacy Project (GULP) and optical data from the Legacy ExtraGalactic UV Survey (LEGUS). We investigated the surroundings of our targets within the range of projected distances expected for runaway stars, 74 pc and 204 pc.

Results. We find that between 9.8% and 34.6% of our targets have no young stellar groups or massive stars within the threshold radii, making them appear isolated. This fraction reduces to 3.2% - 11.5% when we consider the total number of massive stars expected from the observed UV star formation rate.

Conclusions. Our results show that there is a small population of young and massive, potentially isolated field stars in NGC 4242.

Key words. stars: formation / stars: massive / ultraviolet: stars / galaxies: stellar content

1. Introduction

Although small in number, massive stars are powerful engines that affect the local star formation activity of the host galaxy,

quenching star formation in their neighborhood (due to stellar winds or supernova explosions, e.g. Westmoquette et al. 2008) or triggering new star formation episodes at larger distances (a

supernova explosion can compress the interstellar medium, triggering star formation, e.g. Deharveng et al. 2009). Moreover, they are key agents of galactic chemical evolution.

Lada & Lada (2003) show that stars usually form in clustered structures via the collapse and fragmentation of a giant molecular cloud. In massive rich OB clusters, García & Mermilliod (2001) further show that O stars are frequently found in multiple or binary systems. Given their short lifetimes and their usual low velocity, high-mass stars usually do not have enough time to move away from their parental star clusters or OB associations, where they formed. However, Oey et al. (2004) show that up to 35% of the massive stars in the Small Magellanic Cloud (SMC) are located in the field, while Gies (1987) finds a fraction of 22% for the Milky Way (MW). Do these findings imply that massive stars can also form in isolation?

The competitive accretion model of star formation predicts that the formation of a high-mass star requires the presence of a population of low-mass stars (Bonnell et al. 2004). In this scenario, the fragmentation of the parental molecular cloud produces only low-mass cores, some of which compete to accrete the remaining gas, producing high-mass stars. The mass of the most massive object (m_{max}) is then connected to the mass of the resulting cluster (M_{cl}) via $M_{cl} \propto m_{max}^{1.5}$ (Bonnell et al. 2004). In contrast, the core accretion model of star formation allows highmass stars to form in isolation (Krumholz et al. 2009). In this case, the heat produced by the accretion of gas onto a stellar core can be absorbed by the cloud, and this can prevent the further fragmentation of the parental molecular gas cloud. If the column density of the latter is high enough, a monolithic collapse of the clump could happen, leading to the formation of a single massive star. The feedback produced by massive stars has been proposed by Elmegreen & Lada (1977) to trigger the formation of massive stars. In this model, the ionization front coming from an already formed group of massive stars compresses the neutral gas layers, heating them and inducing the formation of a new group of stars (e.g. Zavagno et al. 2006). The higher thermal Jeans mass in the irradiated layers would favor the formation of more massive stars, whereas the formation of low-mass stars will proceed independently and spread out over the cloud. However, this proposal contradicts observations in the Scorpius-Centaurus OB association (Sco-Cen, Preibisch & Zinnecker 2007) which show that low-mass T Tauri stars are coeval with the OB population. More recently, Ratzenböck et al. (2023) reconstructed the star formation history of Sco-Cen using Gaia data, revealing a coherent and sequential pattern of clusters in space and time reminiscent of the scenario proposed by Elmegreen & Lada (1977). However, they did not address the initial mass function of the sequentially formed clusters nor whether low- and high-mass stars could originate from distinct formation channels. In the context of ionization-triggered star formation as in Elmegreen & Lada (1977), it is plausible that an early-formed single massive star suppresses subsequent star formation through its feedback, thus ending up isolated. We note that the model of Elmegreen & Lada (1977) investigates only the formation of the new group of massive stars, leaving the formation process of the first massive stars undisputed. A more detailed review of high-mass formation theories and observations is presented in Zinnecker & Yorke (2007).

Previous investigations of the OB field star population in the SMC have shown that the field population is dominated by runaway OB stars from parental star clusters or OB associations (Dorigo Jones et al. 2020). In fact, OB stars can be ejected from their parental star cluster/OB association via two main possible mechanisms: the dynamical ejection scenario (DES), in which strong gravitational interactions in the cluster core can slingshot

Table 1. Log of observations

Obs. Date	Instrument	Filter	Total Exposure Time
(yy mm dd)			(s)
13 Feb 2021	HST/ACS	F150LP	5400
29 Apr 2021	HST/WFC3	F218W	2160
12 Apr 2014	HST/WFC3	F275W	2376
12 Apr 2014	HST/WFC3	F336W	1116
12 Apr 2014	HST/WFC3	F438W	962
12 Apr 2014	HST/WFC3	F555W	1140
12 Apr 2014	HST/WFC3	F814W	986

Notes. Observation dates, instruments, filters and total exposure times for the used drizzled images.

a massive star into the field (Blaauw 1961; Poveda et al. 1967), and the binary supernova scenario (BSS), in which the supernova explosion of the most massive star in a binary system can eject its high-mass companion (Blaauw 1961; Renzo et al. 2019). More recently, Polak et al. (2024) have proposed a third scenario, the subcluster ejection scenario (SCES). In the hierarchical formation of a star cluster, subclusters merge and form a single cluster. However, during the merging process, a subcluster can fall into the contracting central gravitational potential of the proto cluster, being disrupted by the gravitational force, and ejecting its own stars as runaways in tidal tails.

By definition, the minimum 3D peculiar velocity of a runaway is 30 km s⁻¹ (Gies 1987; Hoogerwerf et al. 2001), which translates into a transverse 2D velocity of 24 km s⁻¹ assuming equal velocity components in space (Dorigo Jones et al. 2020). These velocities imply that the runaway star can travel from tens to hundreds of parsec from its birthplace. Thus, understanding how many O-type stars in the field could be interpreted as runaways and traced back to their parental cluster as opposed to the number of truly isolated massive stars that formed in-situ in isolation becomes crucial in star formation theory and evolution.

Observations in the Milky Way suggest that $4\% \pm 2\%$ of all O stars may be truly isolated from known star clusters/OB associations and can not be attributed to runaways (de Wit et al. 2004, 2005). Recently, Zarricueta Plaza et al. (2023) observed an O3If* that appears isolated in the field, with no evidence of clustering of low-mass stars. Moreover, they excluded the runaway nature from its 2D kinematics. In the Small Magellanic Cloud, Oey et al. (2013) analyzed 14 isolated OB stars, finding that 9 stars show a small overdensity of low-mass stars around them, while the remaining 5 have no clustering and are candidates for in-situ star formation. Lamb et al. (2010), analyzing 8 possible isolated OB stars in the SMC, found that 3 of them show clustering of low-mass stars, 2 were runaways and 3 remained isolated. Vargas-Salazar et al. (2020) found that 4 - 5%of their field O-type star sample in the SMC were not runaways but were surrounded by small clustering of low-mass stars. Thus, they argued that the O stars that appear isolated are, in fact, the "tip of the iceberg" of very sparse star clusters.

In this work, we use far-ultraviolet to optical photometry to identify possible massive and young field stars in NGC 4242, and analyze their surroundings, studying the isolation of each target with respect to young star clusters, OB associations or other massive stars. The paper is organized as follows. Section 2 describes the observations and catalogs; the color-magnitude diagrams and extinction law analysis are presented in Section 3, while the analysis on the isolation is presented in Section 4. The discussion and the conclusions are presented in Section 5 and 6.

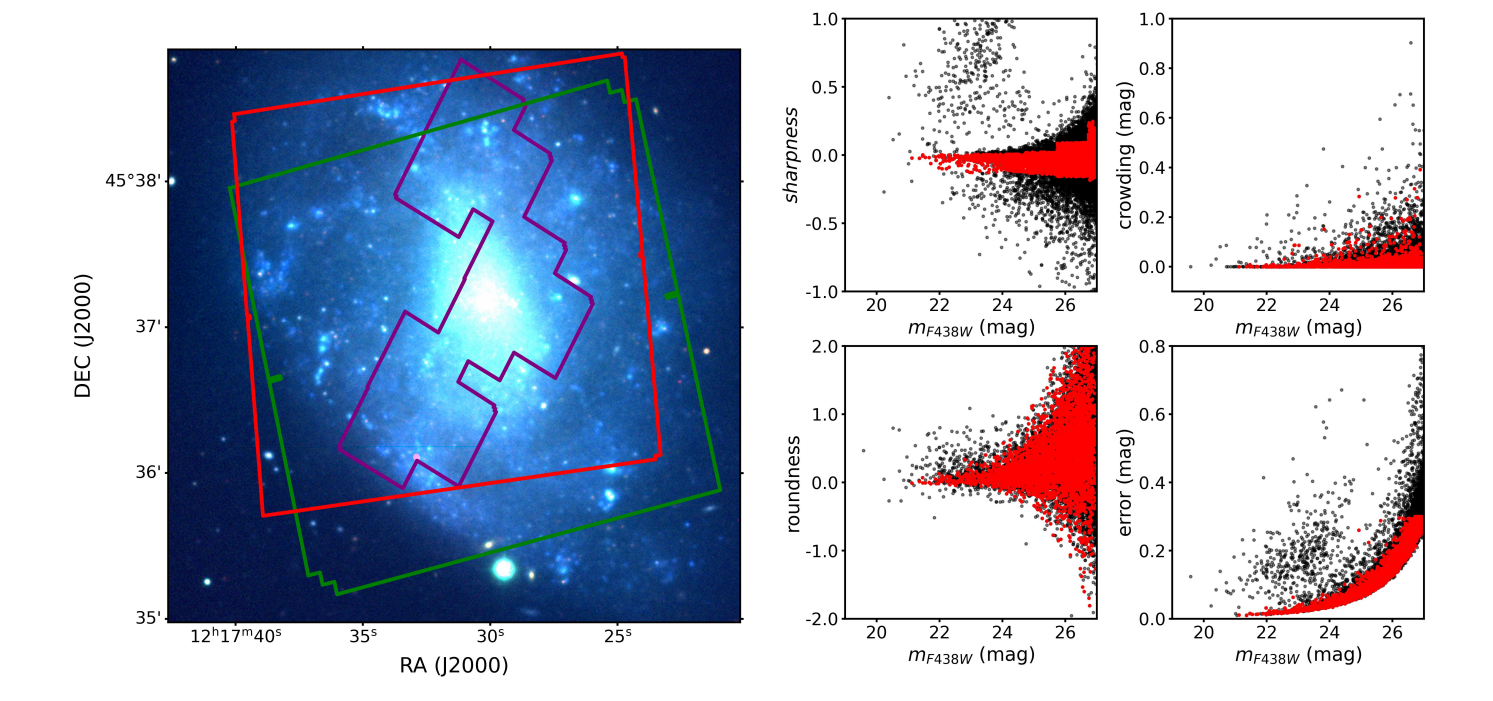


Fig. 1. Optical image of NGC 4242 using the *grz* filters from the Legacy Survey DR6 (Dey et al. 2019) and the GULP (F150LP in purple, F218W in green) and LEGUS (F275W in red) mosaics.

Fig. 2. Quality of the PSF photometry for the sources detected by LE-GUS in the F438W (B) filter. In each panel, black dots refer to the full sample, while red points indicate sources that passed the full selection process as described in Section 2.1.

2. NGC 4242 and data description

We study the unbarred spiral galaxy (SAd) NGC 4242 located at RA(J2000) = 12:17:30.18, DEC(J2000) = +45:37:9.51. The galaxy has a photometric estimated metallicity of Z = 0.02, and is located at a distance of 5.3 Mpc (Sabbi et al. 2018).

The galaxy is part of the star forming galaxies studied by Lee et al. (2011), who derived a star formation rate (SFR) over the past 100 Myr of $\sim 0.09 M_{\odot}$ yr⁻¹ using the far-ultraviolet emission detected by GALEX, corrected for the Galactic dust attenuation using the maps of Schlegel et al. (1998), and a distance of 7.43 Mpc (Kennicutt et al. 2008).

The face-on orientation of NGC 4242 makes the galaxy an excellent benchmark for the search for isolated massive stars. A more strongly inclined orientation, instead, would have required probing the distribution of massive stars through the stellar disc, likely rich in dust, which would have considerably affected the UV observations used in this paper.

The images of NGC 4242 for our analysis were obtained using the Hubble Space Telescope's (HST) Solar Blind Channel of the Advanced Camera for Surveys F150LP filter (FUV) and the UVIS channel of the Wide Field Camera 3 (UVIS/WFC3) filter F218W (MUV) from the Galaxy UV Legacy Project (GULP, PI Sabbi, GO-16316). Moreover, we used UVIS/F275W (NUV), F336W (U), F438W (B), F555W (V) and F814W (I) images from the HST Legacy ExtraGalactic UV Survey (LEGUS, PI Calzetti, GO-13364, Calzetti et al. 2015) to extend the photometric coverage from the far-ultraviolet to the optical wavelengths. Figure 1 shows the FUV, MUV and NUV mosaics used in this paper.

While the UV filters can be used to detect young massive stars, star clusters, and OB associations, the wide photometric coverage helps us to better constrain the spectral energy distributions (SEDs) between $\sim 1500 \mbox{\normalfont\AA}$ and $\sim 8100 \mbox{\normalfont\AA}$ of these high-mass stars, resulting in better estimates of their age and

mass. Furthermore, the UV-filters are key factors to quantify how strongly/efficiently ultraviolet light emitted by massive stars is absorbed by dust grains.

The observing dates, instruments, filters and exposure times are reported in Table 1. All the frames were aligned to Gaia Data Release 3 (Gaia Collaboration et al. 2021) and drizzled to a common pixel scale of 0.04"/px (the native WFC3 pixel size), using the F438W frame as reference.

Fluxes for point-like sources in the F275W, F336W, F438W (reference frame), F555W and F814W filters were measured via PSF-fitting using the WFC3 module of the photometry package DOLPHOT version 2.0 (Dolphin 2000, 2016) The list of stars detected by DOLPHOT in the F275W filter was then used as input to perform aperture photometry in the filters F150LP and F218W using the Astropy package Photutils (Sabbi et al. in prep.). The aperture radius around each object is 3 pixel, and an annulus with an inner radius 12 pixels and a width of 2 pixels is used for sky subtraction. All the magnitudes are in the Vegamag system.

2.1. The stellar photometric catalog

To correctly study the properties of massive stars, we need to remove as many extended objects or spurious detections as possible. We did this in two steps. First, we applied selection criteria on the photometric error, sharpness, and roundness of objects observed in the F438W and F555W filters. All sources with a photometric error larger than 0.3 mag and |roundness|>2 were removed. A further constraint was put on the sharpness: objects whose sharpness deviates more than 1σ from the 50th-percentile value per magnitude bin were discarded. Figure 2 shows how the quality of the photometry changes as a function of the magnitude

in the B filter. The black points represent the full catalog while red points show the sources that passed the full selection process.

As a second step, out of the sources that passed the criteria above, we considered only those with a flux detection in the F275W filter. Stars that were observed in one or both FUV and MUV filters were selected only if their photometric errors in these filters are smaller than 0.3 mag. At the end of the selection phase, we have: sources that are observed only in LEGUS filters (from the NUV to the I band), stars that are observed in all the filters (from the FUV to the I band), and sources with only one GULP flux. In fact, for this galaxy, GULP and LEGUS observations do not completely overlap and we did not want to miss any massive star candidates (see Figure 1).

2.2. Star cluster and OB-association catalog

The LEGUS collaboration identified candidate star clusters and OB associations in the star forming galaxies observed by the survey (Adamo et al. 2017; Grasha et al. 2017). We summarize their procedure here.

An automatic pipeline extracted candidates and computed the concentration index (CI). The concentration index is defined as the magnitude difference between apertures at radii of 1 pixel and 3 pixels. A sample of isolated and bright stars was used to set the threshold CI value between stars and candidate star clusters. For NGC 4242, the threshold value was 1.3 mag for the WFC3 F555W filter. The CI cut allows the user to remove a large amount of stars from the catalog. However, compact and unresolved candidate star clusters whose effective radius is 1 pc or smaller, can be potentially removed by the CI cut. Multi-band aperture photometry and averaged aperture corrections were performed for each target whose CI is larger than the threshold value. In order to remove possible outliers, the sources from the automatic catalog were visually inspected. All the candidates that were observed in at least four bands, with a photometric error smaller than 0.3 mag and whose F555W absolute magnitude is brighter than -6 mag were visually inspected. During the visual inspection, sources that were clearly clusters and were missed during the automatic procedure were added to the catalog. The visually inspected sources were then divided in four classes. Class 1 objects are centrally concentrated objects whose full width at half maximum (FWHM) is more extended than that of a star. Class 2 objects have a less symmetric distribution of light while Class 3 objects are characterized by a multi-peak distribution of their light. Finally, Class 4 objects are potentially single stars or artifacts.

The physical properties of the candidates (such as age, mass and dust extinction) were obtained using SED fitting techniques described in Adamo et al. (2017). In this work, we used the catalog based on Yggdrasil SSP models (Zackrisson et al. 2011) with a Kroupa initial mass function (IMF) (Kroupa 2001), nebular continuum+emission lines with a covering factor 0.5, metallicity Z=0.02, Padova isochrones (Marigo et al. 2008; Girardi et al. 2010; Tang et al. 2014; Chen et al. 2015) and Milky Way extinction law (Cardelli et al. 1989). Figure 3 shows the mass and age distribution of Class 1 + Class 2 and Class 3 objects. In particular, it shows that a large fraction of clusters at young ages (\leq 15 Myr) are low-mass. This trend will be used in Section 4 to refine the cluster sample.

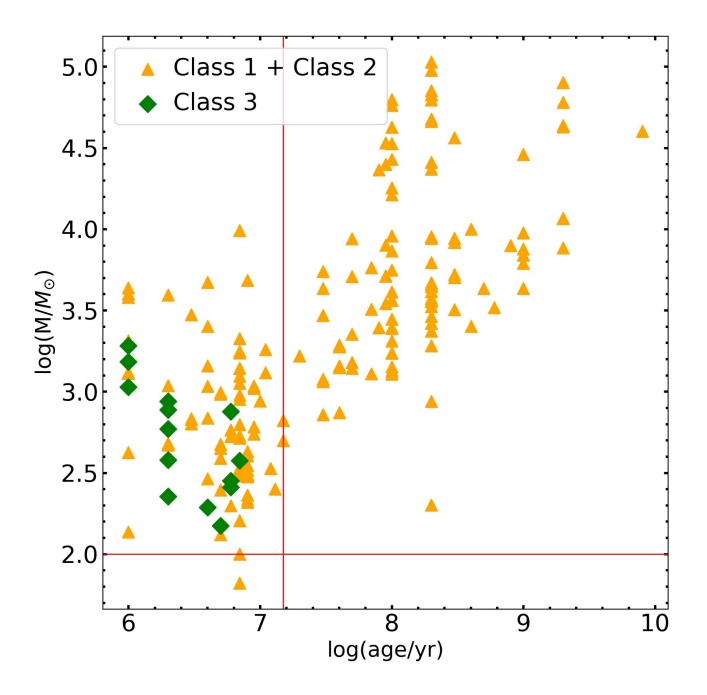


Fig. 3. Mass and age distribution of clusters/OB associations identified by the LEGUS collaboration using the theoretical models described in Section 2.2. The red lines correspond to the $100M_{\odot}$ cut-off and the 15 Myr cut-off used in Section 4.

2.3. $H\alpha$ and infrared images

In order to explore the environment around our massive star candidates, we used auxiliary $H\alpha$ and infrared images. In particular, we used the already stellar-continuum subtracted $H\alpha$ image taken by Kennicutt et al. (2008) with the Bok Telescope to identify the ionized regions around massive stars.

For the dust distribution in NGC 4242, we used the infrared maps obtained by Dale et al. (2009) using the Spitzer Telescope: the Infrared Array Camera (IRAC) 8.0 µm image provides the information on the polycyclic aromatic hydrocarbon (PAH) molecules, while the Multiband Imaging Photometer (MIPS) 24.0 μ m maps show the hot dust. We removed the star emission to get the pure PAH and hot dust emission using the 3.6 μ m as continuum. We computed the stellar PSF of the 3.6, 8.0 and 24.0 μ m images. The pixel scale for the 3.6 and 8.0 μ m data is 0.75"/px, while it is 1.5"/px for the $24.0 \mu m$ data. We convolved the 3.6 μ m image with the 8.0 μ m PSF and the 8 μ m image with the 3.6 μ m PSF using the IRAF function convolve. In order to account for the different pixel scale of the 24.0 μ m image, we first magnified the 3.6 μ m image and PSF using the magnify function in IRAF, and then convolved it with the 24 μ m image and PSF. The convolved images were then subtracted using the equation presented by Helou et al. (2004) and Dale et al. (2009):

$$v f_v (8.0 \,\mu\text{m})_{dust} = v f_v (8.0 \,\mu\text{m}) - \eta^{8*} \, v f_v (3.6 \,\mu\text{m}),$$
 (1)

and similarly for the 24.0 μ m image, where ν is the frequency, f_{ν} is the specific flux density, $\eta^{8*}=0.232\times3.6/8.0$ for the 8.0 μ m image and $\eta^{24*}=0.032\times3.6/24.0$ for the 24.0 μ m map. We will refer to these stellar continuum-subtracted images as "pure" H α , 8.0 μ m and 24.0 μ m images.

3. Massive stars identification and characterization

Color-magnitude diagrams (CMDs) are useful tools for interpreting the resolved stellar component in the host galaxy. Massive stars show the peak of their emission at ultraviolet wavelengths, making them bright objects in the UV filters of the GULP and LEGUS surveys. However, the dust component of the host galaxy absorbs a large fraction of the ultraviolet light, re-emitting it at longer wavelengths. Moreover, different empirical extinction laws for different environments have been found. Thus, it is crucial to determine the correct extinction law for NGC 4242 in order to interpret the properties of its massive stars.

3.1. Extinction Law

How extinction changes as a function of the wavelength was measured for a number of galaxies including the Milky Way (Cardelli et al. 1989; Fitzpatrick 1999) and the Magellanic Clouds (Nandy & Morgan 1978; Gordon et al. 2003; Maíz Apellániz & Rubio 2012). While the MW extinction law exhibits a bump in the absorption of photons at a wavelength of 2175Å (the so-called UV-bump), the SMC extinction law does not.

We first removed the Galactic foreground extinction using Cardelli et al.'s (1989) extinction law and a value of A_V = 0.033 mag (Schlafly & Finkbeiner 2011). We then used the mixture model from Gordon et al. (2016) with a Milky Way and a Small Magellanic Cloud component to see how the extinction affects the photometry of our data. This model depends on the total-to-selective extinction ratio, R_V , and f_A which regulates the amount of extinction due solely to the Milky Way component (see Gordon et al. 2016). We chose the R_V and f_A parameters by visually inspecting the V-I and UV Hess diagrams in two steps. First, we varied the R_V value to match the V-I Hess diagram. Then, keeping R_V fixed, we fine-tuned the f_A parameter trying to match the blue edge in the FUV-B and MUV-B Hess diagrams. We found that the distribution of stars in different Hess diagrams (from the FUV to the I band) is well described by Padova isochrones (Marigo et al. 2008; Girardi et al. 2010; Tang et al. 2014; Chen et al. 2015) using a true distance modulus $\mu = 28.61$ mag, an intrinsic extinction of E(B - V) = 0.05mag and a metallicity Z = 0.02 (Sabbi et al. 2018) for the pair $(R_V, f_A) = (3.1, 1.0)$. This corresponds to the Milky Way extinction law (Fitzpatrick 1999 with $R_V = 3.1$) for NGC 4242. Figure 4 shows the aforementioned Hess diagrams with overplotted Padova isochrones corrected for extinction using $R_V = 3.1$ and $f_A = 1.0$.

3.2. Age Separation

We decided to differentiate stars according to their age estimated via the F150LP vs. F150LP-F814W, F814W vs. F150LP-F814W, F218W vs. F218W-F814W and F275W vs. F275W-F814W CMDs. Figure 5 shows the four different CMDs using Padova isochrones and the extinction parameters from Section 3.1. Stars were divided in age ranges according to their position within two consecutive isochrones.

We are only interested in massive and young objects, so we removed all the objects with an initial mass smaller than $15M_{\odot}$ from each CMD. Using Padova isochrones and a foreground Milky Way extinction $A_V = 0.033$ mag (Schlafly & Finkbeiner 2011), we removed all the objects fainter than 24.7, 21.4, 22.2 and 21.8 mag for the F814W, F150LP, F275W and F218W filters, respectively. Schneider et al. (2018) analyzed 173 O stars in 30 Doradus finding an average maximum age

of about 10 Myr. We therefore decided to consider objects in the age range 1 - 10 Myr. Stars that are bluer than the 1 Myr isochrone (possibly due to photometric errors, uncertainty on the metallicity, the extinction law, and theoretical models) were also taken into account. At this point, stars that are younger than 10 Myr and brighter than the magnitude cut in at least one of these CMDs are considered. We selected 242 objects from the four CMDs. Assuming that these objects are single non-rotating stars, we estimated their initial mass (M_{ini}) , age and intrinsic extinction (A_V) based on their photometry minimizing the difference between observed and theoretical magnitudes. Let y_{obs} and σ be the vectors of the observed magnitudes and photometric errors, and \mathbf{y}_{th} the vector of synthetic reddened magnitudes derived from Padova isochrones. In the theoretical models, the age varies between 1 and 10 Myr with steps of 0.2 Myr, M_{ini} varies between 0.08 and $350M_{\odot}$ and A_V ranges from 0.0 to 1.0 mag with steps of 0.01 mag. We computed the χ^2 for the single model as

$$\chi^2 = \sum_{i=1}^{n_{filters}} \frac{(y_{obs,i} - y_{th,i})^2}{\sigma_i^2}$$
 (2)

and the sum is done over the number of filters. The minimum χ^2 gave the best (logt, M_{ini} , A_V) triplet. To estimate the error on each parameter, we perturbed the observed photometry of each star using a multivariate normal distribution, $\mathcal{N}(\mu = \mathbf{y}_{obs}, \sigma^2 = \sigma^2)$, centered on the observed photometry and with the photometric errors as its σ . We ran 100 Monte Carlo iterations for each star and took the standard deviations of the 100 best triplets as the corresponding errors of each parameter.

The χ^2 confirmed that 234 sources are younger than 10 Myr and with an initial mass larger than 15 M_{\odot} : 100 stars have fluxes available in all filters, 110 with only one GULP flux available and the rest (24) with only LEGUS fluxes (see Section 2.1 and Figure 1).

Figure 6 shows the best values obtained for A_V , age and M_{ini} color-coded by the degree of freedom (dof = 4 for complete wavelength coverage, dof = 3 for only one GULP flux and dof = 2 for detection only in between the NUV and the I bands). The histograms show that the age and A_V of our selected stars are distributed throughout the age range and the 0.0 to 1.0 mag interval, with a mean age of 5.7 Myr and an average intrinsic extinction of $A_V = 0.18$ mag, which is in agreement with Sabbi et al. (2018). The majority of our stars have M_{ini} between 15 and $100M_{\odot}$, with some of them exceeding $M_{ini} = 150M_{\odot}$ and $A_V = 0.4$ mag. A possible explanation for the latter is the presence of a star cluster around our targets or other unresolved stars that can contaminate the photometry. In fact, some of our targets are close to star clusters identified by LEGUS (see Adamo et al. 2017), making the χ^2 higher and the parameter estimate less precise.

In order to test how our derived stellar ages, initial masses and dust extinctions depend on the metallicity of the isochrone and on the extinction law assumed for NGC 4242, we fitted the observed photometry using three different setups: Padova isochrones with SMC metallicity reddened with MW extinction law, Padova isochrones with solar metallicity and SMC extinction law ($R_V = 2.74$ Gordon et al. 2003), and Padova isochrones with SMC metallicity and SMC extinction law. We found that, at fixed metallicity, the average age of our sample becomes younger by 1 Myr and the average extinction slightly increases by 0.01 mag, while at fixed extinction law, the population becomes older by 1 Myr and the extinction increases not more than 0.02 mag. The results are described in Appendix A.

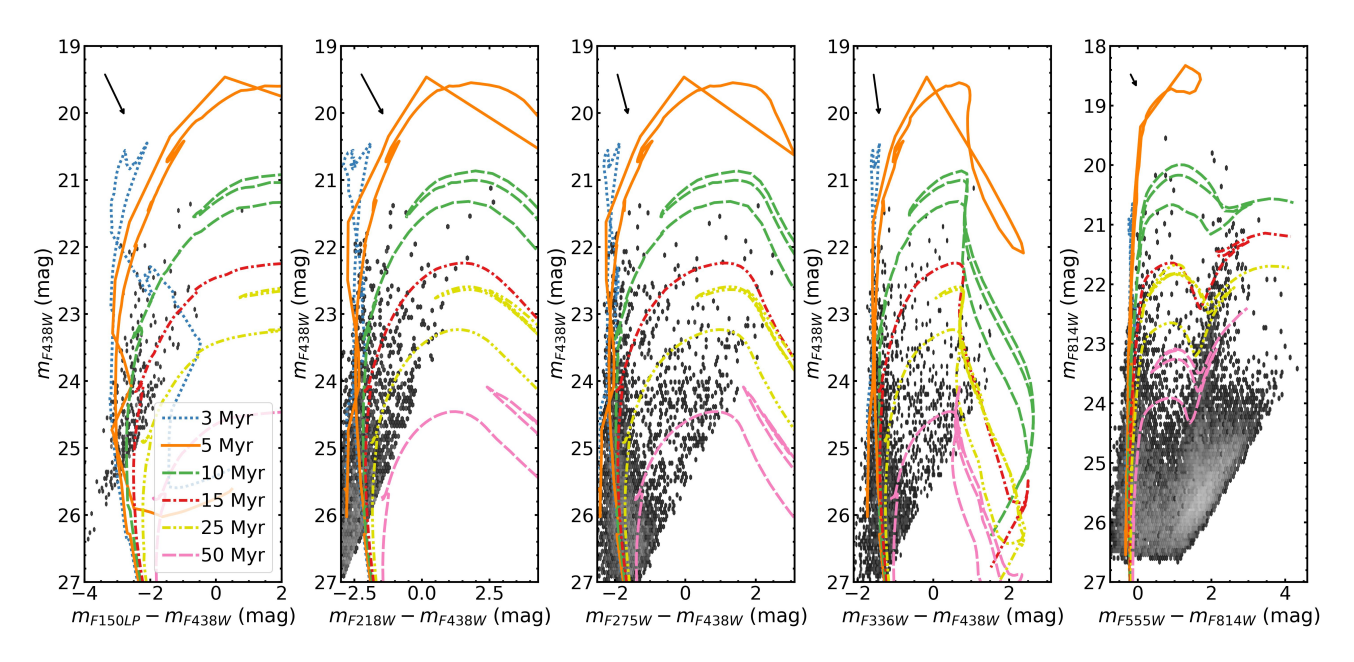


Fig. 4. Hess diagrams for different combinations of filters. Padova isochrones for different ages are overplotted, using Z = 0.02, E(B - V) = 0.05 mag, distance modulus $\mu = 28.61$ mag (Sabbi et al. 2018) and the extinction coefficients from the Gordon et al. (2016) model with $R_V = 3.1$ and $f_A = 1.0$. The black arrow indicates the reddening vector using $A_V = 0.5$ mag.

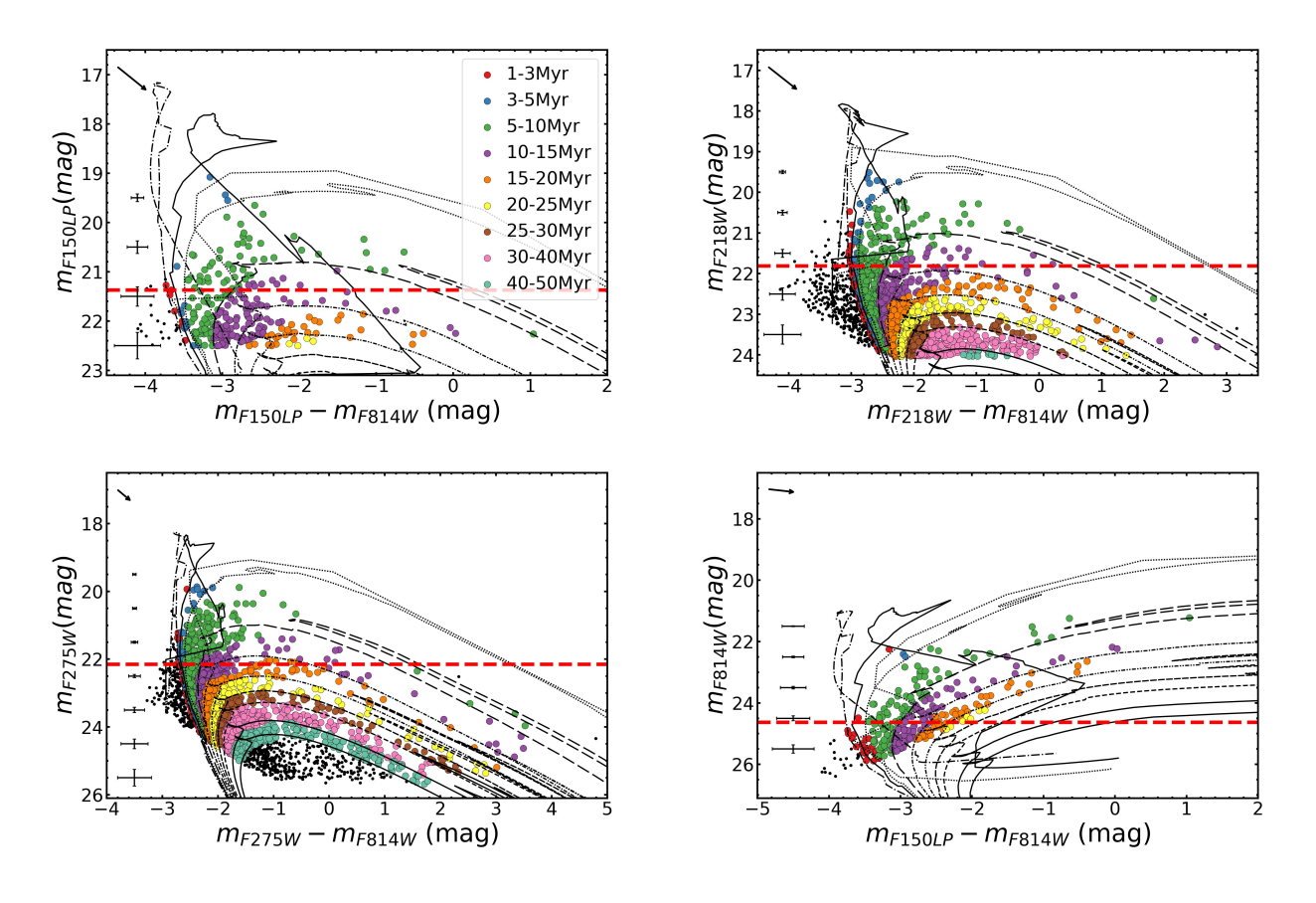


Fig. 5. CMDs used to differentiate stars according to age. Padova isochrones for ages 1, 3, 5, 10, 15, 20, 25, 30, 40, 50 Myr, metallicity Z= 0.02, distance modulus $\mu = 28.61$ mag and intrinsic E(B-V)= 0.05 mag are superimposed. The extinction coefficients come from Gordon et al. (2016) model with $R_V = 3.1$ and $f_A = 1.0$. Stars are color-coded by the age determined by their positions between consecutive isochrones in each CMD. The black points are stars that do not lie in between consecutive isochrones. The dashed red line shows the luminosity of a main sequence star with $M_{ini} = 15 M_{\odot}$ and an age of 10 Myr. The black arrow indicates the reddening vector using $A_V = 0.1$ mag.

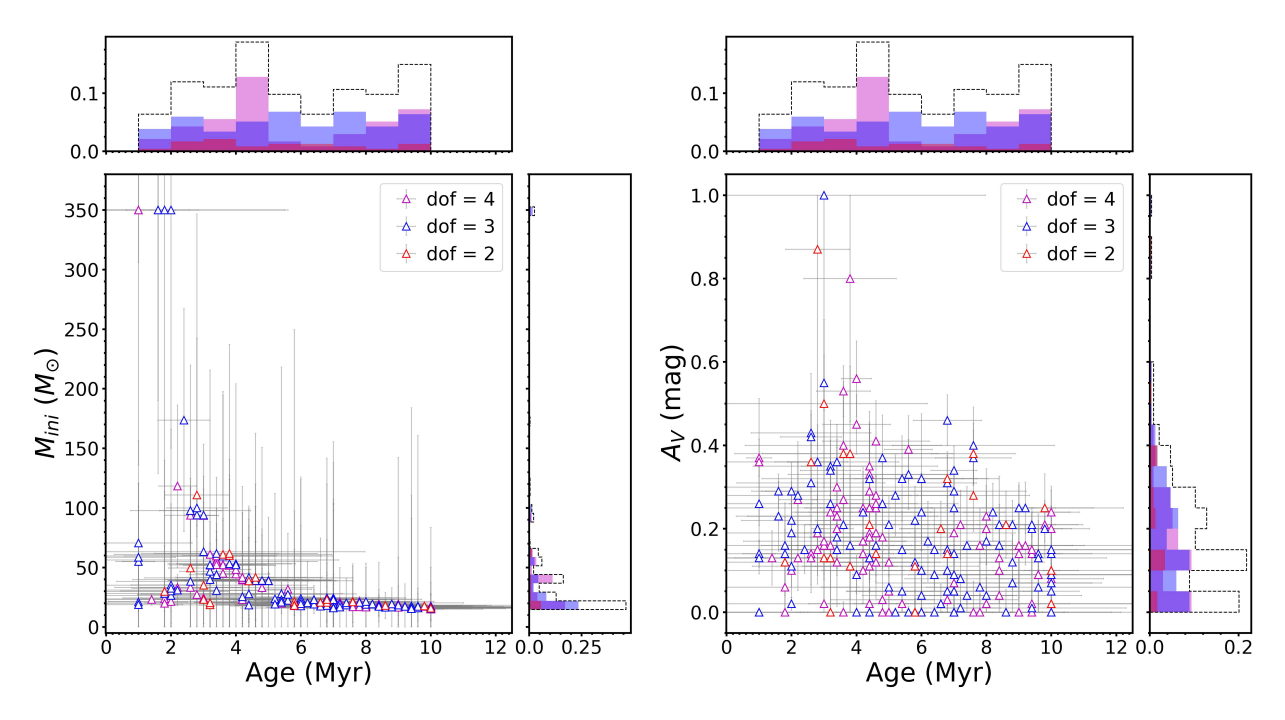


Fig. 6. Best values for age, A_V and M_{ini} and their histogram distributions using Padova isochrones with a fixed metallicity Z = 0.02, an age range of 1 - 10 Myr and a varying intrinsic extinction $A_V \in [0.0, 1.0]$ based on the extinction coefficients from Gordon et al. (2016) for $R_V = 3.1$ and $f_A = 1.0$ (Section 3.1). The targets are divided in three groups based on the degrees of freedom, which depend on the number of available filters as explained in Section 2.1 (dof = 4 for complete wavelength coverage, dof = 3 for only one GULP flux and dof = 2 for detection only in between the NUV and the I bands). The histograms are normalized to the total number of sources. The black dashed histogram shows the total frequency.

3.3. Spatial distribution of the targets

We expect to find massive and young objects along the spiral arms of NGC 4242. Figure 7 shows the spatial distribution of the targets grouped in four different age bins. We use the stellar continuum subtracted H α image taken by Kennicutt et al. (2008) with the Bok Telescope to connect young targets with H α emission (drawn in magenta). The comparison between Figure 1 and 7 shows that most of the targets are distributed along the faint spiral arms of NGC 4242, as delineated by the H α emission in Figure 7.

In most of the cases, our targets are located in $H\alpha$ emission regions. The left panel of Figure 8 shows the spatial distribution of the targets color-coded by the best values for their reddening. We note that some targets need a very small reddening even if they coincide with $H\alpha$ emission. We suggest that these targets are not in the $H\alpha$ emission region, but they are in the foreground and the $H\alpha$ is in the background within the galaxy NGC 4242. On the other hand, some targets with a high reddening are not associated with $H\alpha$ emission. It is possible that stars with a high value for the reddening are behind dust lanes. The right panel of Figure 8 shows a composite image of the pure $H\alpha$ emission (in magenta), the pure $8.0~\mu m$ (in green) and the pure $24.0~\mu m$ (in orange). The dust images were taken by the Spitzer Space Telescope (Dale et al. 2009) and the stellar continuum subtraction is described in Section 2.3.

4. Isolation analysis

4.1. Isolation with respect to star clusters or OB associations

Even if massive stars are short-lived, those in the field are frequently considered to be runaways or walkaways from known star clusters or OB associations (Blaauw 1961; Poveda et al. 1967; Gies 1987; Hoogerwerf et al. 2001; Dorigo Jones et al.

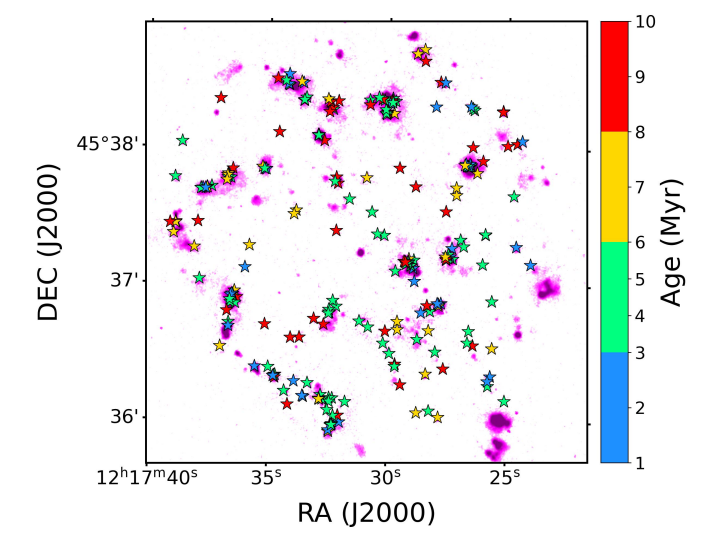


Fig. 7. Spatial distribution of the selected targets grouped in four different age bins. The underlying pure $H\alpha$ emission (in magenta) is taken by Kennicutt et al. (2008) with the Bok Telescope.

2020). Thus, we looked at the spatial distribution of our targets and the visually inspected young star clusters (age \leq 15 Myr) from Adamo et al. (2017) (see Section 2.2) to see how many stars from our sample could potentially be runaways from star clusters. We note here that while in the MW and the SMC, the runaway or walkaway nature of a star can be tested via spectroscopic radial velocities and astrometric tangential velocities, this is not feasible with the existing instrumentation in a galaxy at the distance of NGC 4242.

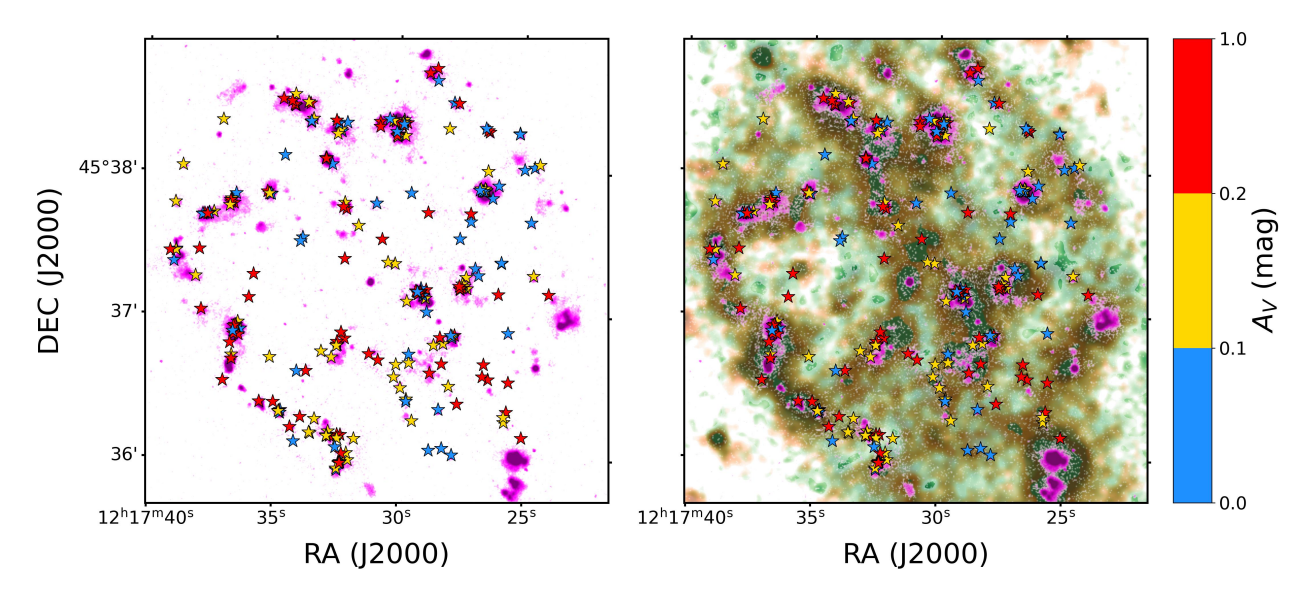


Fig. 8. Spatial distribution of the targets color-coded by the best value of their intrinsic extinction A_V . On the left panel the pure Hα emission is drawn in magenta. On the right panel, the underlying pure Hα is in magenta, the pure 8.0 μm in green (PAH emission), and the pure 24.0 μm in orange (hot dust emission).

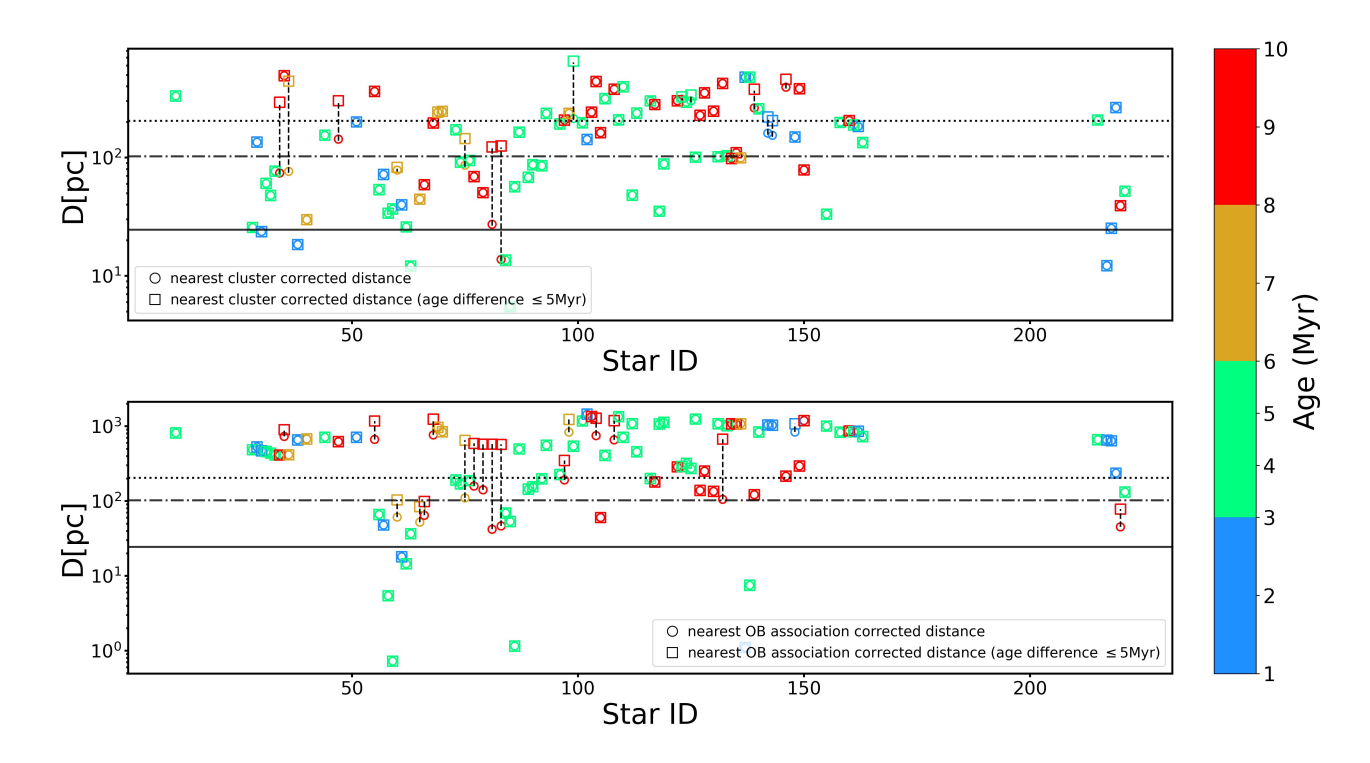


Fig. 9. De-projected distances between stars with dof = 4 and star clusters (top panel) or OB associations (bottom panel). On the x axis the star ID from the sample is shown. The circle symbols show the distance of the closest cluster from each target (Method 1), while the squares show the closest cluster with an age similar to that of each star (Method 2). The black dashed vertical lines connect the distances from Method 1 and Method 2 when they find two different stellar groups. The symbols are color-coded accordingly to the derived age of the stars. The gray horizontal lines show the maximum tangential distances that a star can travel in 1 Myr with a constant velocity of 24 km s⁻¹, 100 km s⁻¹ and 200 km s⁻¹. These distances are 24, 102 and 204 pc (horizontal solid, dot-dashed and dotted lines, respectively). At a distance of 5.3 Mpc, 1 pc is 0.039 arcsec.

The clusters can be divided in three classes, depending on their PSF shape: spherically symmetric, asymmetric, or multipeak PSF (see Section 2.2). In this work, we grouped together symmetric and asymmetric objects and we will refer to these objects as star clusters, while multipeak PSF objects will be considered OB associations due to their larger extensions. We decided

to consider only objects more massive than $100M_{\odot}$. In fact, using Gaia data, Hunt & Reffert (2023) were able to identify Galactic open clusters as massive as $\sim 100M_{\odot}$ containing few massive stars as massive as $50M_{\odot}$. In NGC 4242 we have 74 young (≤ 15 Myr) star clusters and only 14 OB associations, with a median separation of ~ 180 pc.

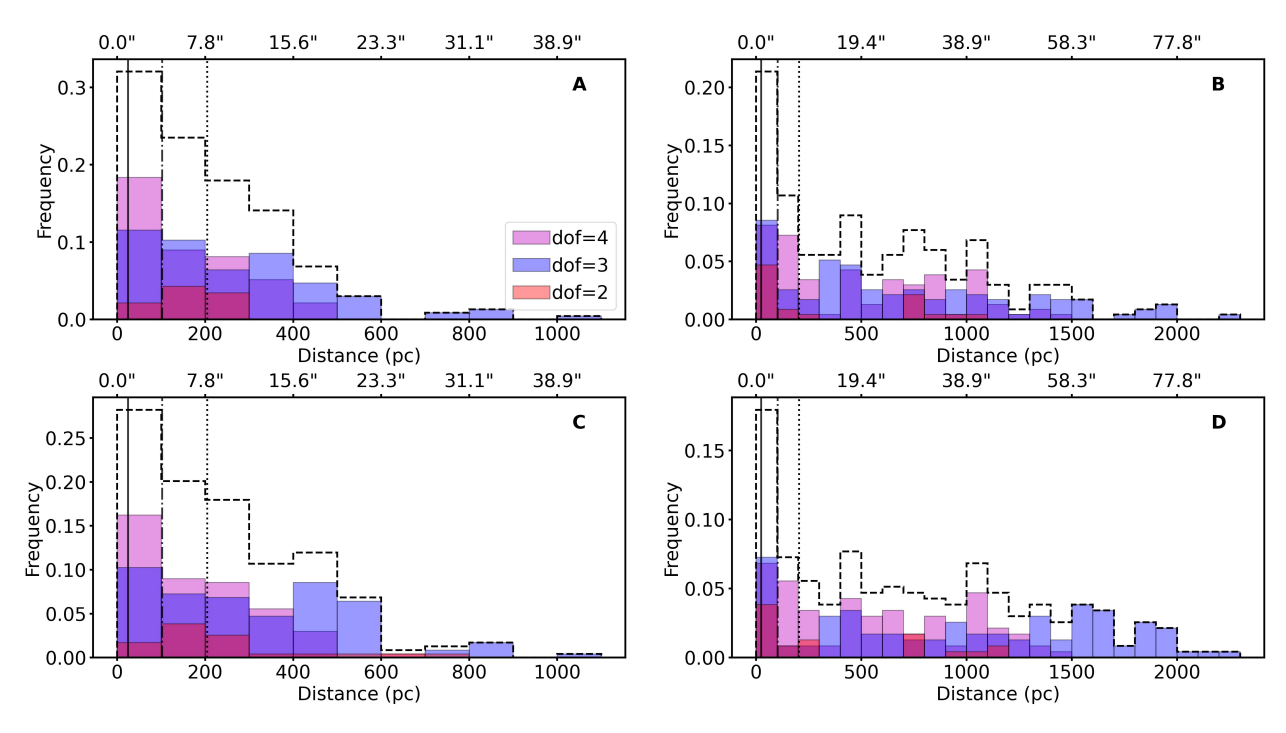


Fig. 10. Distance distributions: panels A and B show the simple projected 2D distance between our stars and the nearest star cluster and OB association, respectively; panels C and D show the distances from the nearest star cluster or OB associations differing from estimated stellar ages by 5 Myr at most. The sample is color-coded accordingly to the degree of freedom and each histogram is normalized to the total number of stars in the sample. The dashed black histogram shows the total frequency. All bins have equal size of 100 pc. The black vertical lines show the distances that a star can travel in 1 Myr with a constant velocity of 24 km s^{-1} , 100 km s^{-1} and 200 km s^{-1} . These distances are 24, 102 and 204 pc.

Runaway OB stars can be produced via two main mechanisms: the dynamical ejection scenario and the binary supernova scenario. In the former, gravitational interactions in dense clusters could eject a massive star (Blaauw 1961; Poveda et al. 1967), while in the latter the supernova explosion could eject the companion star (Renzo et al. 2019; Blaauw 1961). Recently, Polak et al. (2024) have analyzed the production of runaways through the subclusters ejection mechanism, where stars in a subcluster can be ejected during the tidal disruption of the parent subcluster falling into the deeper gravitational potential of the proto cluster. Runaway stars are traditionally defined to have a 3D peculiar motion of at least 30 km s⁻¹ (Gies 1987; Hoogerwerf et al. 2001), which corresponds to a transverse 2D minimum velocity of 24 km s⁻¹ assuming equal velocity components in space (Dorigo Jones et al. 2020). Fast runaways with a velocity of 200 km s⁻¹ in the SMC have been found by Dorigo Jones et al. (2020), however, theoretical studies (Perets & Šubr 2012) show that the runaway frequency is strongly reduced with increasing peculiar velocity. This is in agreement with Dorigo Jones et al. (2020), who found that only 48 stars out of 199 runaway stars in the SMC have local velocities larger than 75 km s⁻¹, showing that the peak of the distribution of runaway stars is reached between 30 and 75 km s⁻¹ with a steep drop for higher velocities. A steep decrease in the distribution of runaway stars was also found for the massive star cluster R136 in the Large Magellanic Cloud (Stoop et al. 2024), with only 8 (out of 23) O-type stars being runaways from R136 with tangential velocities larger than 50 km s⁻¹. Taking these velocities as references, a runaway star can travel tens to hundreds of parsecs in a few Myr. For example, Stoop et al. (2024) found that the population of O runaway stars has traveled a mean distance of 59 pc from the center of R136, with this value reaching a value of 115 pc considering also the runaways without a spectral classification. The theoretical studies on the BSS done by Renzo et al. (2019) revealed that a main sequence massive companion star travels on average ~ 75 pc, in agreement with the 50 pc found by Eldridge et al. (2011). However, both distributions of the maximum distance are characterized by a large scatter.

We looked at the closest star cluster or OB association from each star target, and addressed the question "How probable is it that our target belongs to that star cluster?". We de-projected the positions of stars and star clusters on the galaxy plane adopting an inclination of $i = 40.5^{\circ}$ (Calzetti et al. 2015) and then computed their 2D projected distance.

In order to take into account the velocity distribution found by Dorigo Jones et al. (2020), we decided to take two threshold distances: $d_{thresh,1} = 74$ pc and $d_{thresh,2} = 204$ pc. The former corresponds to the distance traveled by a star in 1 Myr with three times the minimum 2D runaway velocity, while the latter is the distance that a fast runaway can travel in 1 Myr at 200 km s⁻¹. These two threshold distances allowed us not only to identify runaway candidates with the former velocities and 1 Myr travel time, but also runaways with a combination of velocities and travel times. For example, the $d_{thresh,2}$ can help identify runaway stars with the minimum 2D runaway velocity that have traveled for ~ 8 Myr.

Every star that has a star cluster/OB association closer than the threshold distance can be considered as possible walkaway or runaway from that particular group, otherwise it is in isolation (thereafter Method 1). Each circle in Figure 9 shows the location of the closest star cluster/OB association for each star with dof= 4. However, finding a star near to a star cluster does not imply that they are connected. We decided to look also at the age information: given the age of the star, we selected star clusters whose age differs by 5 Myr at most from the age of the star, and then searched for the closest cluster (thereafter Method 2). The 5 Myr range takes into account the age spread of Otype stars found in Cygnus OB2 (Berlanas et al. 2020) and in the

Table 2. Number and frequency of possible isolated stars with respect to the closest star clusters or OB associations.

Sample	Method 1		Me	thod 2
$d_{thresh,1} = 74pc$	Number	Frequency	Number	Frequency
only clusters				
dof=4	70	0.299	72	0.308
dof=3	86	0.368	90	0.385
dof=2	19	0.081	20	0.085
whole sample	175	0.748	182	0.778
only OB associations				
dof=4	81	0.346	87	0.372
dof=3	92	0.393	94	0.402
dof=2	15	0.064	16	0.068
whole sample	188	0.803	197	0.842
clusters + OB associations				
dof=4	66	0.282	69	0.295
dof=3	80	0.342	85	0.363
dof=2	13	0.056	15	0.064
whole sample	159	0.679	169	0.722
$d_{thresh,2} = 204 pc$	Number	Frequency	Number	Frequency
only clusters				
dof=4	35	0.149	40	0.171
dof=3	57	0.244	68	0.291
dof=2	9	0.038	11	0.047
whole sample	101	0.432	119	0.509
only OB associations				_
dof=4	64	0.274	71	0.303
dof=3	84	0.359	91	0.389
dof=2	11	0.047	13	0.056
whole sample	159	0.679	175	0.748
clusters + OB associations				
dof=4	26	0.111	33	0.141
dof=3	49	0.209	62	0.265
dof=2	4	0.017	8	0.034
whole sample	79	0.338	103	0.440

Notes. Number and frequency of possible isolated stars (with respect to the closest star clusters or OB associations) given the threshold distance of $d_{thresh,1} = 74$ pc and $d_{thresh,2} = 204$ pc. Method 1 takes into account only the de-projected positions of stars and clusters, while Method 2 considers clusters whose age difference with the stars is 5 Myr at most. The frequencies are normalized to the total sample of stars.

massive star cluster R136 (Schneider et al. 2018). Moreover, it corresponds to the maximum error on the age of our stars computed in Section 3.2. In fact, the mean error on the age of a stars from the isochrone fitting is 1.8 Myr, while the maximum error is 5 Myr. We chose the latter as the maximum age difference between a stars and a cluster to create possible connections between them. Each square in Figure 9 shows where the closest star cluster/OB association is located for each star with a similar age. The stars are divided into age bins. The two methods for the distances in some cases found the same connection between star and clusters (no connecting dashed line), while there are some stars that appear to be close to a star cluster whose age difference is more than 5 Myr, making their connections less likely true, and increasing their chance to be unrelated to those clusters.

Following the age bins in Figure 9, we computed the median separation between stars and their nearest cluster/OB association using Method 1 and 2. For the star clusters we found a positive correlation, with the median distance between young stars and star clusters increasing towards older age bins; however, this trend becomes weaker for Method 2. On the other hand, for younger age bins, OB associations are found to be closer to young stars with the trend disappearing using Method 2. The dif-

ferent trend between clusters and OB associations is most likely due to the small number statistics of the latter.

In Figure 10 we show how many connections between star and star clusters/OB associations we are able to find as a function of the projected distance. The figure shows that there is a population of stars that are found far away from known star clusters or OB associations, being potentially isolated. Table 2 summarizes the number of isolated objects given the method or the threshold value. Note that some of our stars could have traveled a longer distance (with a higher runaway velocity or for longer time), and may contaminate the isolated star sample. Conversely, stars in projected proximity to clusters or OB associations may be unrelated to them.

4.2. Isolation with respect to other massive stars

Another criterion for the isolation is that no other massive and young object is found in the vicinity of each target. Following Dorigo Jones et al. (2020) and Renzo et al. (2019), we also investigated the isolation of each target with respect to other massive and young stars from our sample. We decided to consider the Method 1 and the two threshold distances as constraint for the isolation from other massive stars. Table 3 shows the num-

Table 3. Number of possible isolated stars with respect to the closest star clusters, OB associations and massive stars.

Sample	Me	Method 1		thod 2
	Number	Frequency	Number	Frequency
clusters + OB associations ($d_{thresh,1}$)				
and stars $(d_{thresh,1})$ isolation				
dof=4	31	0.132	31	0.132
dof=3	42	0.179	43	0.184
dof=2	6	0.026	7	0.029
whole sample	79	0.338	81	0.346
clusters + OB associations ($d_{thresh,1}$)				
and stars $(d_{thresh,2})$ isolation				
dof=4	6	0.026	6	0.026
dof=3	20	0.085	20	0.085
dof=2	2	0.009	2	0.009
whole sample	28	0.120	28	0.120
clusters + OB associations ($d_{thresh,2}$)				
and stars $(d_{thresh,1})$ isolation				
dof=4	15	0.064	17	0.073
dof=3	29	0.124	33	0.141
dof=2	2	0.009	5	0.021
whole sample	46	0.197	55	0.235
clusters + OB associations ($d_{thresh,2}$)				
and stars $(d_{thresh,2})$ isolation				
dof=4	4	0.017	4	0.017
dof=3	17	0.073	18	0.077
dof=2	2	0.009	2	0.009
whole sample	23	0.098	24	0.103

Notes. Number of possible isolated stars (with respect to the closest star clusters, OB associations and massive stars) given the threshold distance of $d_{thresh,1} = 74$ pc and $d_{thresh,2} = 204$ pc. Method 1 takes into account only the de-projected positions of stars and clusters, while Method 2 considers clusters whose age difference with the star is 5 Myr at most. The frequencies are normalized to the total sample of stars.

ber of objects that have no known star clusters and other massive and young stars nearby for different threshold distances. The new constraint implies a reduction in the isolation frequencies. However, it can be seen that, whatever the method of distances and the threshold value, the final frequency of potentially isolated objects is never zero.

This final sample may contain two types of objects: stars that could have been formed in-situ in the field in isolation (or with a small population of low-mass stars around them) and possible runaways that traveled for a larger period of time than the travel times that we considered or with higher velocities.

5. Discussion

We investigated the environment around 234 young massive star candidates in order to study the phenomenon of possible isolated massive star formation. In the previous section we examined the possibility that some of our targets could be runaways from known star clusters or OB associations. Whether runaway objects are produced via binary supernova, dynamical ejection, or subcluster ejection mechanisms, their peculiar velocity in the galaxy plane is at least 24 km s⁻¹ (Dorigo Jones et al. 2020). Considering this velocity as typical velocity of runaways, we set $d_{thresh,1} = 74$ pc as the first threshold distance a runaway can typically travel, finding with Method 1 that $68\% \pm 6\%$ (= 159/234) of the stars in the sample lie at a larger distance and have no known young star clusters/OB associations around them.

However, there is evidence that some stars could reach very high runaway velocities (Dorigo Jones et al. 2020; Sana et al. 2022). In order to remove possible fast runaways from our sam-

ple, we adopted $d_{thresh,2} = 204$ pc as our second threshold distance. As a consequence, the fraction of possible isolated stars with respect to star clusters and OB associations using Method 1 decreases to $34\% \pm 4\%$ (= 79/234).

The fact that we set the minimum threshold ($d_{thresh,1}$) to three times the distance a runaway star can travel in 1 Myr at the minimum 2D velocity not only enables the selection of stars potentially moving at higher velocities or for longer times, but also accounts for the ~ 0.5 Mpc uncertainty in the distance of NGC 4242 (Sabbi et al. 2018). For very high velocities, the number of very fast runaways drops sharply with the velocity (Perets & Subr 2012; Dorigo Jones et al. 2020). Increasing $d_{thresh,2}$ would lead to a large number of connections between stars and clusters, not all of which are necessarily true. In fact, we expect to miss only few faster runaways, given their low number. Moreover, these two threshold distances allowed us not only to identify runaway candidates traveling for only 1 Myr at the two constant velocities, but also runaways with a combination of velocities and travel times.

The possible connections between stars and stars cluster were based only on the projected distance. If instead one looks also at the similarity in age between stars and star clusters, the number of possible physical connections decreases. We assumed a maximum age difference between a star and a star cluster of 5 Myr. This age difference reflects the age spread that Berlanas et al. (2020) and Schneider et al. (2018) found for massive stars in Cygnus OB2 and R136, respectively. Moreover, 5 Myr corresponds to the maximum age error we obtained for our sample, and is consistent with the age discrepancy of 0.2 dex found by Stevance et al. (2020) between single-star isochrone and bi-

nary SED fitting with BPASS (Binary Population and Spectral Synthesis). This uncertainty will affect only Method 2, while the results from Method 1 will be unaffected.

Ten (for $d_{thresh,1}$) or twenty-four (for $d_{thresh,2}$) stars that we previously associated with star clusters or OB associations as possible runaways, differ more than 5 Myr from those clustering, making these links less likely to be physical. The resulting fractions of possible isolated objects using Method 2 become $72\% \pm 6\% \ (= 169/234)$ and $44\% \pm 4\% \ (= 103/234)$ for $d_{thresh,1}$ and $d_{thresh,2}$, respectively.

A further constraint is the isolation with respect to other massive stars outside of clusters. Depending on the threshold distance and method, the frequency can vary from a minimum of $9.8\% \pm 2\%$ (= 23/234, for $d_{thresh,2}$ and Method 1) to a maximum of $34.6\% \pm 3\%$ (= 81/234, for $d_{thresh,1}$ and Method 2). The errors are for Poisson statistics only.

Observations suggest that $4\% \pm 2\%$ of all O-stars in the Milky Way appear to be isolated from known star clusters/OB associations and can not be interpreted as runaways (de Wit et al. 2005). This result is consistent with Vargas-Salazar et al. (2020) who found that 4-5% of O-type stars in the field of the Small Magellanic Cloud appear to be isolated from star clusters/OB associations, but these authors also observed small clustering of low-mass stars around these seemingly isolated massive stars. Parker & Goodwin (2007) found that the fraction of sparse star clusters ($M < 100M_{\odot}$) with only one massive O-type star can vary between 1.3% and 4.6% for a cluster mass function exponent of $\beta = 1.7$ and $\beta = 2$, respectively.

In order to compare our findings with those of de Wit et al. (2005), we computed the expected number of massive stars $(M_{ini} \ge 15 M_{\odot})$ that have not undergone a SN explosion at 10 Myr. We computed the SFR(UV) directly from the the GALEX FUV image (Lee et al. 2009) in the F275W HST footprint, using the equation presented in Kennicutt (1998), a distance of 5.3 Mpc, and correcting for the Galactic foreground extinction from Schlafly & Finkbeiner (2011). These resulted in a SFR(UV)=0.038 \dot{M}_{\odot} yr⁻¹. We corrected this star formation rate for the intrinsic mean extinction found in Section 3.2. The final star formation rate is SFR(UV)= $0.057M_{\odot} \text{ yr}^{-1}$. We also estimated the SFR(H α) from the Bok image in the F275W HST footprint, following the flux calibration described in Kennicutt et al. (2008) and using the equation presented in Kennicutt (1998), applying the same distance and foreground and intrinsic extinction corrections (using the mean extinction from Section 3.2 using solar metallicity and a MW-like extinction law), and using the star-to-gas extinction conversion from Calzetti et al. (2000). We found that the SFR(H α) is 57% lower than the SFR(UV), in agreement with the value found by Lee et al. (2009). Different studies of H II regions in galaxies with different metallicities, masses and SFRs have shown that the escape fraction of the ionizing photons can reach values of the order of 67% (Della Bruna et al. 2021; Ramambason et al. 2022; Egorov et al. 2018; Gerasimov et al. 2022; Pellegrini et al. 2012). The large escape fraction can lead to an underestimation of the SFR(H α) of up to a factor of three. Therefore, we decided to assume a constant SFR= $0.057 M_{\odot} \text{ yr}^{-1}$ from the GALEX FUV over the last 100 Myr to compute the expected number of massive stars in our HST footprint. We computed the expected number of massive stars not yet exploded as supernova using the equation presented by Kim et al. (2013):

$$\mathcal{P}_* = \frac{\dot{M}_*}{m_*} \Delta t \tag{3}$$

where $\dot{M}_* = 0.057 M_{\odot} {\rm yr}^{-1}$ is the dust-corrected SFR(UV), $\Delta t = 10$ Myr is our age range, and $m_* = 812 M_{\odot}$ is the total mass in massive stars that have not yet exploded as supernova. The latter was computed using a Kroupa IMF (Kroupa 2001) and a mass range $15-18.88 M_{\odot}$. These two masses are the lower initial mass for our sample and the upper limit for a star that survives for 10 Myr without exploding. We found that the expected number of massive stars in the field and clusters for our mass and age limits to be ~ 707 objects. When we use the expected total number of massive stars, we find that the fraction of possible isolated objects is $3.2 \pm 0.7\% - 11.5 \pm 1.3\%$. The value 11.5% that we find for a threshold of 74 pc is a factor 3 larger than what de Wit et al. (2005) found using a 65 pc threshold.

We re-computed the fraction of candidate isolated massive stars using the stellar parameters obtained in Appendix A for the three different setups described in Section 3.2. For solar metallicity and SMC-like extinction the fractions vary between $2.2\pm0.5\%-7.6\pm0.9\%$ due to a larger average extinction and consequently higher dust-corrected SFR(UV), while the fractions become higher if we assume a SMC-like metallicity with MW-like extinction law $(3.3\pm0.6\%-12.0\pm1.2\%)$. Finally, the combination of a SMC metallicity with the SMC-like extinction law gives fractions in between $2.1\pm0.4\%-7.6\pm0.7\%$ (see Appendix A).

We note that our fractions of isolated massive star candidates are upper limits. In fact, the cluster catalog contains only cluster candidates which were visually inspected and whose effective radius is at least 1 parsec (see Adamo et al. 2017), missing potentially unresolved clusters with sizes of 1 parsec and below. The presence of these compact star clusters can reduce the number of possible isolated objects. On the other hand, this is mitigated by the requirement of avoiding other massive stars around each target. Moreover, the distinction between possible runaways from star clusters and isolated objects is based only on position information and not on local velocities for our targets. In fact, the runaway nature of a star can be tested via spectroscopic radial velocities and astrometric tangential velocities in the MW and SMC, but this is not feasible in a galaxy at the distance of NGC 4242. Therefore, some of our final targets could still be very fast runaways or could have traveled longer from their original birthplace. Finally, some of the isolated candidates may be surrounded by a non-detected stellar clustering of lowmass stars (Vargas-Salazar et al. 2020) that we are not able to detect. Conversely, we may be missing truly isolated stars that are seen to lie close to clusters or OB associations in projection.

6. Conclusions

In summary, we carried out a galaxy-wide search of massive stars throughout the entire galaxy NGC 4242 using far and mid-ultraviolet data from HST to find young massive stars that are isolated with respect to star clusters, OB associations and other massive stars. We first presented the identification of possible single young massive field stars exploiting the F150LP and F218W fluxes from ACS/SBC and WFC3 from HST, identifying 234 candidates. We then analyzed the surroundings of these targets, looking for the presence of young (\leq 15 Myr) star clusters and OB associations identified in the LEGUS survey (Adamo et al. 2017). In fact, massive stars can be ejected from star clusters or OB associations becoming runaways or walkaways.

We set two threshold distances, 74 and 204 pc. The former corresponds to three times the distance a massive star can travel in 1 Myr with the minimum 2D velocity of 24 km s⁻¹, while the latter corresponds to the distance a fast runaway can travel in

the same time interval with a velocity of 200 km s⁻¹. Every star that has a star cluster or OB association closer than the threshold distance could be a potential runaway from that star group. We decided to analyze the isolation of our targets based not only on their positions, but considering also the similarity in age between stars and star clusters/OB associations. In this second method, we looked at the spatial distribution of star clusters and OB associations whose age differs less than 5 Myr from the estimated age of the selected massive star.

The surroundings of the possible isolated objects were then analyzed, looking for the presence of other massive stars. Depending on the method and on the threshold distance, we find a frequency for isolation in the field of NGC 4242 that varies from 9.8% to 34.6%, using $d_{thresh,2}$ and $d_{thresh,1}$, respectively. These fractions reduce to $3.2 \pm 0.7\% - 11.5 \pm 1.3\%$ when computed with respect to the total expected population of massive stars in the galaxy, with the latter a factor three larger than what de Wit et al. (2005) found for the Milky Way. However, our fractions are upper limits to the fraction of truly isolated massive stars. In fact, we cannot probe the possible clustering of low-mass stars around our targets, i.e. we cannot exclude the presence of very sparse star clusters. The fraction of seemingly isolated massive stars around which faint clustering of low-mass stars were found is 4 – 5% in the Small Magellanic Cloud (Vargas-Salazar et al. 2020). Moreover, our results can still be affected by the presence of very fast runaways or objects that have traveled for a longer period of time. Conversely, we may be missing truly isolated stars located in close apparent proximity to star clusters due to projection effects.

This is the first study that searched for isolated massive stars in a galaxy beyond the immediate neighborhood of the Milky Way. Overall, we find a fraction of potentially isolated massive stars similar to the early work for the Milky Way and Magellanic Clouds. Future studies at higher resolution are needed to elucidate this issue further.

Acknowledgements. We thank the anonymous referee for the constructive comments that helped improving the paper. The HST observations used in this paper are associated with program No. 16316 and No. 13364. This work is based on observations obtained with the NASA/ESA Hubble Space Telescope, at the Space Telescope Science Institute, which is operated by the Association of Universities for Research in Astronomy, Inc., under NASA contract NAS 5-26555. E.S. is supported by the international Gemini Observatory, a program of NSF NOIRLab, which is managed by the Association of Universities for Research in Astronomy (AURA) under a cooperative agreement with the U.S. National Science Foundation, on behalf of the Gemini partnership of Argentina, Brazil, Canada, Chile, the Republic of Korea, and the United States of America. J.S.G acknowledges grant support under these GO programs from the Space Telescope Science Institute which is operated by the Association of Universities for Research in Astronomy, Inc., under NASA contract NAS 5-26555. A.A acknowledges support from Vetenskapsrådet 2021-05559. RSK acknowledges financial support from the ERC via Synergy Grant "ECOGAL" (project ID 855130), from the German Excellence Strategy via the Heidelberg Cluster "STRUCTURES" (EXC 2181 - 390900948), and from the German Ministry for Economic Affairs and Climate Action in project "MAINN" (funding ID 50002206). RSK also thanks the 2024/25 Class of Radcliffe Fellows for highly interesting and stimulating discussions. The Legacy Surveys consist of three individual and complementary projects: the Dark Energy Camera Legacy Survey (DECaLS; Proposal ID #2014B-0404; PIs: David Schlegel and Arjun Dey), the Beijing-Arizona Sky Survey (BASS; NOAO Prop. ID #2015A-0801; PIs: Zhou Xu and Xiaohui Fan), and the Mayall z-band Legacy Survey (MzLS; Prop. ID #2016A-0453; PI: Arjun Dey). DECaLS, BASS and MzLS together include data obtained, respectively, at the Blanco telescope, Cerro Tololo Inter-American Observatory, NSF's NOIR-Lab; the Bok telescope, Steward Observatory, University of Arizona; and the Mayall telescope, Kitt Peak National Observatory, NOIRLab. Pipeline processing and analyses of the data were supported by NOIRLab and the Lawrence Berkeley National Laboratory (LBNL). The Legacy Surveys project is honored to be permitted to conduct astronomical research on Iolkam Du'ag (Kitt Peak), a mountain with particular significance to the Tohono O'odham Nation.

References

Adamo, A., Ryon, J. E., Messa, M., et al. 2017, ApJ, 841, 131

```
Adamo, A., Ryon, J. E., Messa, M., et al. 2017, ApJ, 841, 131
Berlanas, S. R., Herrero, A., Comerón, F., et al. 2020, A&A, 642, A168
Blaauw, A. 1961, Bull. Astron. Inst. Netherlands, 15, 265
Bonnell, I. A., Vine, S. G., & Bate, M. R. 2004, MNRAS, 349, 735
Calzetti, D., Armus, L., Bohlin, R. C., et al. 2000, ApJ, 533, 682
Calzetti, D., Lee, J. C., Sabbi, E., et al. 2015, AJ, 149, 51
Cardelli, J. A., Clayton, G. C., & Mathis, J. S. 1989, ApJ, 345, 245
Chen, Y., Bressan, A., Girardi, L., et al. 2015, MNRAS, 452, 1068
Dale, D. A., Cohen, S. A., Johnson, L. C., et al. 2009, ApJ, 703, 517
de Wit, W. J., Testi, L., Palla, F., Vanzi, L., & Zinnecker, H. 2004, A&A, 425,
 de Wit, W. J., Testi, L., Palla, F., & Zinnecker, H. 2005, A&A, 437, 247
Deharveng, L., Zavagno, A., Schuller, F., et al. 2009, A&A, 496, 177
Della Bruna, L., Adamo, A., Lee, J. C., et al. 2021, A&A, 650, A103
Dey, A., Schlegel, D. J., Lang, D., et al. 2019, AJ, 157, 168
Dolphin, A. 2016, DOLPHOT: Stellar photometry, Astrophysics Source Code
         Library, record ascl:1608.013
  Dolphin, A. E. 2000, PASP, 112, 1383
 Dorigo Jones, J., Oey, M. S., Paggeot, K., Castro, N., & Moe, M. 2020, ApJ,
         903, 43
 Egorov, O. V., Lozinskaya, T. A., Moiseev, A. V., & Smirnov-Pinchukov, G. V.
         2018, MNRAS, 478, 3386
 Eldridge, J. J., Langer, N., & Tout, C. A. 2011, MNRAS, 414, 3501
Elmegreen, B. G. & Lada, C. J. 1977, ApJ, 214, 725
Fitzpatrick, E. L. 1999, PASP, 111, 63
 Gaia Collaboration, Brown, A. G. A., Vallenari, A., et al. 2021, A&A, 649, A1 Gallazzi, A., Charlot, S., Brinchmann, J., White, S. D. M., & Tremonti, C. A.
         2005, MNRAS, 362, 41
 García, B. & Mermilliod, J. C. 2001, A&A, 368, 122
Gerasimov, I. S., Egorov, O. V., Lozinskaya, T. A., Moiseev, A. V., & Oparin,
        D. V. 2022, MNRAS, 517, 4968
 Gies, D. R. 1987, ApJS, 64, 545
Girardi, L., Williams, B. F., Gilbert, K. M., et al. 2010, ApJ, 724, 1030
Gordon, K. D., Clayton, G. C., Misselt, K. A., Landolt, A. U., & Wolff, M. J.
Gordon, K. D., Clayton, G. C., Misselt, K. A., Landolt, A. U., & Wolff, M 2003, ApJ, 594, 279
Gordon, K. D., Fouesneau, M., Arab, H., et al. 2016, ApJ, 826, 104
Grasha, K., Calzetti, D., Adamo, A., et al. 2017, ApJ, 840, 113
Helou, G., Roussel, H., Appleton, P., et al. 2004, ApJS, 154, 253
Hoogerwerf, R., de Bruijne, J. H. J., & de Zeeuw, P. T. 2001, A&A, 365, 49
Hunt, E. L. & Reffert, S. 2023, A&A, 673, A114
Kennicutt, Robert C., J., Lee, J. C., Funes, J. G., et al. 2008, ApJS, 178, 247
Kennicutt, Jr., R. C. 1998, ARA&A, 36, 189
Kim, C.-G., Ostriker, E. C., & Kim, W.-T. 2013, ApJ, 776, 1
Kroupa, P. 2001, MNRAS, 322, 231
Krumholz M. R., Klein, R. I., McKee, C. F., Offner, S. S. R., & Cunningh,
  Krumholz, M. R., Klein, R. I., McKee, C. F., Offner, S. S. R., & Cunningham,
          A. J. 2009, Science, 323, 754
 A. J. 2009, Science, 323, 754
Lada, C. J. & Lada, E. A. 2003, ARA&A, 41, 57
Lamb, J. B., Oey, M. S., Werk, J. K., & Ingleby, L. D. 2010, ApJ, 725, 1886
Lee, J. C., Gil de Paz, A., Kennicutt, Jr., R. C., et al. 2011, ApJS, 192, 6
Lee, J. C., Gil de Paz, A., Tremonti, C., et al. 2009, ApJ, 706, 599
Maíz Apellániz, J. & Rubio, M. 2012, A&A, 541, A54
Marigo, P., Girardi, L., Bressan, A., et al. 2008, A&A, 482, 883
Nandy, K. & Morgan, D. H. 1978, Nature, 276, 478
Oey, M. S., King, N. L., & Parker, J. W. 2004, AJ, 127, 1632
Oey, M. S., Lamb, J. B., Kushner, C. T., Pellegrini, E. W., & Graus, A. S. 2013,
ApJ, 768, 66
          ApJ, 768, 66
 ApJ, 708, 00
Parker, R. J. & Goodwin, S. P. 2007, MNRAS, 380, 1271
Pellegrini, E. W., Oey, M. S., Winkler, P. F., et al. 2012, ApJ, 755, 40
Perets, H. B. & Subr, L. 2012, ApJ, 751, 133
Polak, B., Mac Low, M.-M., Klessen, R. S., et al. 2024, A&A, 690, A207
Poveda, A., Ruiz, J., & Allen, C. 1967, Boletin de los Observatorios Tonantzintla
 y Tacubaya, 4, 86
Preibisch, T. & Zinnecker, H. 2007, in IAU Symposium, Vol. 237, Triggered Star
 Formation in a Turbulent ISM, ed. B. G. Elmegreen & J. Palous, 270–277 Ramambason, L., Lebouteiller, V., Bik, A., et al. 2022, A&A, 667, A35 Ratzenböck, S., Großschedl, J. E., Alves, J., et al. 2023, A&A, 678, A71 Renzo, M., Zapartas, E., de Mink, S. E., et al. 2019, A&A, 624, A66 Sabbi, E., Calzetti, D., Ubeda, L., et al. 2018, ApJS, 235, 23
  Sana, H., Ramírez-Agudelo, O. H., Hénault-Brunet, V., et al. 2022, A&A, 668,
  Schlafly, E. F. & Finkbeiner, D. P. 2011, ApJ, 737, 103
 Schlegel, D. J., Finkbeiner, D. P., & Davis, M. 1998, ApJ, 500, 525
Schneider, F. R. N., Ramírez-Agudelo, O. H., Tramper, F., et al. 2018, A&A,
         618, A73
  Stevance, H. F., Eldridge, J. J., McLeod, A., Stanway, E. R., & Chrimes, A. A.
 2020, MNRAS, 498, 1347
Stoop, M., de Koter, A., Kaper, L., et al. 2024, Nature, 634, 809
   Tang, J., Bressan, A., Rosenfield, P., et al. 2014, MNRAS, 445, 4287
 Vargas-Salazar, I., Oey, M. S., Barnes, J. R., et al. 2020, ApJ, 903, 42
Westmoquette, M. S., Smith, L. J., & Gallagher, J. S. 2008, MNRAS, 383, 864
Zackrisson, E., Rydberg, C.-E., Schaerer, D., Östlin, G., & Tuli, M. 2011, ApJ,
         740, 13
 Zarricueta Plaza, M. S., Roman-Lopes, A., & Sanmartim, D. 2023, A&A, 675,
 Zavagno, A., Deharveng, L., Comerón, F., et al. 2006, A&A, 446, 171 Zinnecker, H. & Yorke, H. W. 2007, ARA&A, 45, 481
```

Appendix A: The effect of different metallicity and dust models on the isolation results

Following the mass-metallicity relation from Gallazzi et al. (2005) and given the mass $M = 1.2 \cdot 10^9 M_{\odot}$, we decided to explore how our results change when we select stars and fit their SEDs using isochrones computed for Z = 0.004 (SMClike metallicity). Using the foreground galactic extinction A_V = 0.033 mag (Schlafly & Finkbeiner 2011), the new magnitude cuts for $M = 15M_{\odot}$ become 25.2, 21.4, 22.5 and 22.1 mag for F814W, F150LP, F275W and F218W filters, respectively. Following the analysis method from Section 3.2 and the extinction law from Gordon et al. (2016) with $R_V = 3.1$ and $f_A = 1.0$, we found 306 possible massive and young stars outside known clusters and associations. The fainter magnitude cuts resulted in a bigger sample of candidates. We re-ran the isochrone-fitting code and found an average age of 8 Myr and a higher average extinction ($A_V = 0.19$ mag) than the results of Section 3.2. Tables A.1, A.2 show the final results for the isolation with respect to cluster and OB associations and the isolation considering also massive stars. We find that the numbers of isolated candidates (and the relative frequencies) stay close to the results in Section 5. At this metallicity, stars with $M_{ini} = 19.96 M_{\odot}$ did not yet explode as SNe, resulting in a total number of expected massive stars of ~ 876 for a corrected star formation rate of SFR(UV)= $0.059M_{\odot} \text{ yr}^{-1}$. Thus, the fraction for the total isolation varies between a minimum of $3.3 \pm 0.6\%$ to a maximum of $12.0 \pm 1.2\%$, slightly higher than the results from Section 5.

A second unknown factor that can affect our analysis is the presence or the absence of the 2175Å UV-bump. We present an analysis using solar metallicity and SMC-like extinction law using $R_V = 2.74$ (Gordon et al. 2003). The resulting sample of possible massive and young field stars is composed of 235 objects. The SMC-like extinction law makes the sample slightly younger with a median age of 4.4 Myr and redder than the MWlike extinction law results. Even if the absence of the 2175Å UVbump could affect the Method 2, the isolation analysis shows no/small changes. In fact, the largest variation between the isolation fraction with and without the 2175Å dust-bump is of the order of 1% (see Table A.3, A.4 for the isolation fraction using Z = 0.02 and $R_V = 2.74$). However, the higher average extinction ($A_V = 0.19$ mag) results in a higher corrected star formation rate, SFR(UV)= $0.085M_{\odot}$ yr⁻¹, and a larger number of expected massive stars (~ 1052). The resulting fractions can vary in the smaller range $2.2 \pm 0.5 - 7.6 \pm 0.9\%$.

Finally, it is straightforward to model our isochrone-fitting technique using a SMC metallicity and SMC-like extinction law. We found 306 possible massive and young field stars: the average age becomes older (5.5 Myr) and the mean extinction $A_V=0.22$ mag. Even if the new set of analyses describes a sample older than the original one, we found only very small changes in the fraction of isolated stars (see Tables A.5, A.6). The higher maximum initial mass to not undergo a SN explosion at 10 Myr at SMC metallicity and the higher extinction result in a corrected star formation rate of $0.094M_{\odot}$ yr⁻¹ and an expected number of massive stars of ~ 1382 . The resulting fraction can vary between $2.1 \pm 0.4 - 7.6 \pm 0.7\%$.

Table A.1. Number of possible isolated stars relative to nearby clusters or OB associations (SMC-like metallicity and MW-like extinction law setup).

	0 1 M 1 11 M 1 10				
Sample	Me	thod 1		thod 2	
$d_{thresh,1} = 74pc$	Number	Frequency	Number	Frequency	
only clusters					
dof=4	93	0.304	104	0.340	
dof=3	117	0.382	123	0.402	
dof=2	23	0.075	23	0.075	
whole sample	233	0.761	250	0.817	
only OB associations					
dof=4	111	0.363	121	0.395	
dof=3	128	0.418	133	0.435	
dof=2	18	0.059	21	0.069	
whole sample	257	0.840	275	0.899	
clusters + OB associations					
dof=4	89	0.291	102	0.333	
dof=3	112	0.366	119	0.389	
dof=2	16	0.052	19	0.062	
whole sample	217	0.709	240	0.784	
$d_{thresh,2} = 204$ pc	Number	Frequency	Number	Frequency	
only clusters					
dof=4	44	0.144	59	0.193	
dof=3	74	0.242	87	0.284	
dof=2	12	0.039	15	0.049	
whole sample	130	0.425	161	0.526	
only OB associations					
dof=4	89	0.291	105	0.343	
dof=3	117	0.382	127	0.415	
dof=2	13	0.042	18	0.059	
whole sample	219	0.716	250	0.817	
clusters + OB associations					
dof=4	34	0.111	52	0.170	
dof=3	65	0.212	79	0.258	
dof=2	6	0.020	13	0.042	
whole sample	105	0.343	144	0.471	

Notes. Number and frequency of possible isolated stars (with respect to the closest star clusters or OB associations) given the threshold distance of $d_{thresh,1} = 74$ pc and $d_{thresh,2} = 204$ pc. Method 1 takes into account only the de-projected positions of stars and clusters, while Method 2 considers clusters whose age difference is 5 Myr at most. The number of stars is 306 using a SMC-like metallicity and a MW-like extinction law.

Table A.2. Number of possible isolated stars relative to nearby clusters, OB associations, and massive stars (SMC-like metallicity and MW-like extinction law setup).

Sample	Method 1		Me	thod 2
	Number	Frequency	Number	Frequency
clusters + OB associations $(d_{thresh,1})$				
and stars $(d_{thresh,1})$ isolation				
dof=4	39	0.127	39	0.127
dof=3	58	0.190	59	0.193
dof=2	7	0.023	7	0.023
whole sample	104	0.340	105	0.343
clusters + OB associations $(d_{thresh,1})$				
and stars $(d_{thresh,2})$ isolation				
dof=4	12	0.039	12	0.039
dof=3	25	0.082	25	0.082
dof=2	3	0.010	3	0.010
whole sample	40	0.131	40	0.131
clusters + OB associations $(d_{thresh,2})$				
and stars $(d_{thresh,1})$ isolation				
dof=4	20	0.065	24	0.078
dof=3	36	0.118	41	0.134
dof=2	3	0.010	5	0.0163
whole sample	59	0.193	70	0.229
clusters + OB associations $(d_{thresh,2})$				
and stars $(d_{thresh,2})$ isolation				
dof=4	9	0.029	9	0.029
dof=3	17	0.056	18	0.059
dof=2	3	0.010	3	0.010
whole sample	29	0.095	30	0.098

Notes. Number of possible isolated stars (with respect to the closest star clusters, OB associations and massive stars) given the threshold distance of $d_{thresh,1} = 74$ pc and $d_{thresh,2} = 204$ pc. Method 1 takes into account only the de-projected positions of stars and clusters, while Method 2 considers clusters whose age difference is 5 Myr at most. The number of stars is 306 using a SMC-like metallicity and a MW-like extinction law.

Table A.3. Number of possible isolated stars relative to nearby clusters or OB associations (solar metallicity and SMC-like extinction law setup).

Sample	Method 1		Me	thod 2
$d_{thresh,1} = 74pc$	Number	Frequency	Number	Frequency
only clusters				
dof=4	70	0.298	70	0.298
dof=3	87	0.370	91	0.387
dof=2	19	0.081	20	0.085
whole sample	176	0.749	181	0.770
only OB associations				
dof=4	81	0.345	83	0.353
dof=3	93	0.396	95	0.404
dof=2	15	0.064	16	0.068
whole sample	189	0.804	194	0.826
clusters + OB associations				
dof=4	66	0.281	66	0.281
dof=3	81	0.345	86	0.366
dof=2	13	0.055	15	0.064
whole sample	160	0.681	167	0.711
$d_{thresh,2} = 204$ pc	Number	Frequency	Number	Frequency
only clusters				
dof=4	35	0.149	41	0.174
dof=3	58	0.247	70	0.298
dof=2	9	0.038	11	0.047
whole sample	102	0.434	122	0.519
only OB associations				
dof=4	64	0.272	68	0.289
dof=3	85	0.362	91	0.387
dof=2	11	0.047	13	0.055
whole sample	160	0.681	172	0.732
clusters + OB associations				
dof=4	26	0.111	33	0.140
dof=3	50	0.213	64	0.272
dof=2	4	0.17	8	0.034
whole sample	80	0.340	105	0.447

Notes. Number and frequency of possible isolated stars (with respect to the closest star clusters or OB associations) given the threshold distance of $d_{thresh,1} = 74$ pc and $d_{thresh,2} = 204$ pc. Method 1 takes into account only the de-projected positions of stars and clusters, while Method 2 considers clusters whose age difference is 5 Myr at most. The number of stars is 235 using a solar metallicity and a SMC-like extinction law.

Table A.4. Number of possible isolated stars relative to nearby clusters, OB associations, and massive stars (solar metallicity and SMC-like extinction law setup).

Sample	Me	Method 1		thod 2
	Number	Frequency	Number	Frequency
clusters + OB associations $(d_{thresh,1})$				
and stars $(d_{thresh,1})$ isolation				
dof=4	31	0.132	31	0.132
dof=3	41	0.174	42	0.179
dof=2	6	0.026	7	0.0298
whole sample	78	0.332	80	0.340
clusters + OB associations $(d_{thresh,1})$				
and stars $(d_{thresh,2})$ isolation				
dof=4	6	0.026	6	0.026
dof=3	20	0.085	20	0.085
dof=2	2	0.009	2	0.009
whole sample	28	0.119	28	0.119
clusters + OB associations ($d_{thresh,2}$)				
and stars $(d_{thresh,1})$ isolation				
dof=4	15	0.064	17	0.072
dof=3	29	0.123	32	0.136
dof=2	2	0.009	5	0.021
whole sample	46	0.196	54	0.230
clusters + OB associations $(d_{thresh,2})$				
and stars $(d_{thresh,2})$ isolation				
dof=4	4	0.017	4	0.017
dof=3	17	0.072	17	0.072
dof=2	2	0.009	2	0.009
whole sample	23	0.098	23	0.098

Notes. Number of possible isolated stars (with respect to the closest star clusters, OB associations and massive stars) given the threshold distance of $d_{thresh,1} = 74$ pc and $d_{thresh,2} = 204$ pc. Method 1 takes into account only the de-projected positions of stars and clusters, while Method 2 considers clusters whose age difference is 5 Myr at most. The number of stars is 235 using a solar metallicity and a SMC-like extinction law.

Table A.5. Number of possible isolated stars relative to nearby clusters or OB associations (SMC-like metallicity and SMC-like extinction law setup).

Sample	Method 1		Method 2	
$\frac{1}{d_{thresh,1} = 74pc}$	Number	Frequency	Number	Frequency
only clusters				
dof=4	93	0.304	98	0.320
dof=3	117	0.382	126	0.412
dof=2	23	0.075	23	0.075
whole sample	233	0.761	247	0.807
only OB associations				
dof=4	111	0.363	117	0.382
dof=3	128	0.418	133	0.435
dof=2	18	0.059	20	0.065
whole sample	257	0.840	270	0.882
clusters + OB associations				
dof=4	89	0.291	94	0.307
dof=3	112	0.366	122	0.399
dof=2	16	0.052	18	0.059
whole sample	217	0.709	234	0.765
$d_{thresh,2} = 204$ pc	Number	Frequency	Number	Frequency
only clusters				
dof=4	44	0.144	52	0.170
dof=3	74	0.242	93	0.304
dof=2	12	0.039	14	0.046
whole sample	130	0.425	159	0.520
only OB associations				
dof=4	89	0.291	100	0.327
dof=3	117	0.382	127	0.415
dof=2	13	0.042	16	0.052
whole sample	219	0.716	243	0.794
clusters + OB associations				
dof=4	34	0.111	43	0.141
dof=3	65	0.212	85	0.278
dof=2	6	0.020	10	0.033
whole sample	105	0.343	138	0.451

Notes. Number and frequency of possible isolated stars (with respect to the closest star clusters or OB associations) given the threshold distance of $d_{thresh,1} = 74$ pc and $d_{thresh,2} = 204$ pc. Method 1 takes into account only the de-projected positions of stars and clusters, while Method 2 considers clusters whose age difference is 5 Myr at most. The number of stars is 306 using a SMC-like metallicity and a SMC-like extinction law.

Table A.6. Number of possible isolated stars relative to nearby clusters, OB associations, and massive stars (SMC-like metallicity and SMC-like extinction law setup).

Sample	Method 1		Me	thod 2
	Number	Frequency	Number	Frequency
clusters + OB associations $(d_{thresh,1})$				
and stars $(d_{thresh,1})$ isolation				
dof=4	39	0.127	39	0.127
dof=3	58	0.190	59	0.193
dof=2	7	0.023	7	0.023
whole sample	104	0.340	105	0.343
clusters + OB associations ($d_{thresh,1}$)				
and stars $(d_{thresh,2})$ isolation				
dof=4	12	0.039	12	0.039
dof=3	25	0.082	25	0.082
dof=2	3	0.010	3	0.010
whole sample	40	0.131	40	0.131
clusters + OB associations ($d_{thresh,2}$)				
and stars $(d_{thresh,1})$ isolation				
dof=4	20	0.065	23	0.075
dof=3	36	0.118	42	0.137
dof=3	3	0.010	3	0.010
whole sample	59	0.193	68	0.222
clusters + OB associations $(d_{thresh,2})$				
and stars $(d_{thresh,2})$ isolation				
dof=4	9	0.029	9	0.029
dof=3	17	0.056	18	0.059
dof=2	3	0.010	3	0.010
whole sample	29	0.095	30	0.098

Notes. Number of possible isolated stars (with respect to the closest star clusters, OB associations and massive stars) given the threshold distance of $d_{thresh,1} = 74$ pc and $d_{thresh,2} = 204$ pc. Method 1 takes into account only the de-projected positions of stars and clusters, while Method 2 considers clusters whose age difference is 5 Myr at most. The number of stars is 306 using a SMC-like metallicity and a SMC-like extinction law.